



## New carbon xerogel-TiO<sub>2</sub> composites with high performance as visible-light photocatalysts for dye mineralization



Esther Bailón-García<sup>a</sup>, Abdelhakim Elmouwahidi<sup>a</sup>, Miguel A. Álvarez<sup>b</sup>, Francisco Carrasco-Marín<sup>a</sup>, Agustín F. Pérez-Cadenas<sup>a</sup>, Francisco J. Maldonado-Hódar<sup>a,\*</sup>

<sup>a</sup> Research Group in Carbon Materials, Inorganic Chemistry Department, Faculty of Sciences, University of Granada, Campus Fuentenueva s/n, 18071 Granada, Spain

<sup>b</sup> Inorganic and Organic Chemistry Department, Faculty of Experimental Sciences, University of Jaén, Campus Las Lagunillas, 23071 Jaén, Spain

### ARTICLE INFO

#### Article history:

Received 25 May 2016

Received in revised form 29 July 2016

Accepted 3 August 2016

Available online 4 August 2016

#### Keywords:

Carbon xerogels

Carbon-TiO<sub>2</sub> composites

Visible photocatalysts

Synergetic effect

### ABSTRACT

A series of carbon xerogels-TiO<sub>2</sub> samples was prepared by sol-gel synthesis, modifying the synthesis procedure to have carbon-TiO<sub>2</sub> composite or TiO<sub>2</sub>-coated materials. Textural, morphological and chemical properties were extensively characterized and correlated with the photocatalytic activity. In the case of composites, a homogeneous and highly mesoporous structure is formed, where the intimate contact between both phases allows a high and homogeneous dispersion of TiO<sub>2</sub> nanoparticles. During carbonization, the formation of oxygen vacancies is favoured, but the transition anatase to rutile is avoided by the carbon matrix. In the case of coated samples, microporous materials structured as microspheres were obtained, TiO<sub>2</sub> present a greater crystal size and some transformation to rutile. The synergetic role of carbon phase and the formation of oxygen vacancies in the TiO<sub>2</sub>-phase contribute to narrow the composite band gap in such a manner that all samples are active under visible radiation reaching the total mineralization of the pollutant and the elimination of the toxicity.

© 2016 Elsevier B.V. All rights reserved.

### 1. Introduction

The increasing pollution level of water resources together with the appearance of new and more stable pollutant in solution (emerging pollutant) make necessary the development of new and more efficient protocols to deal with this new problem. Traditionally, environmental catalysis tries to respond adequately to this requirement, fitting or developing materials and processes for a progressively more industrialized society. A large battery of advanced oxidation processes (Fenton, ozonation, catalytic wet air oxidation (CWAO), etc) is being developed [1–3]. Between them, photocatalytic processes are very interesting, and sometimes are used in combination [4] with the previous ones (photoFenton, photoozonation, etc). Photocatalytic processes become especially interesting when are able to use the visible radiation, not only by the energy saving, but because in such a way can be easily used in developing countries.

It is well known that TiO<sub>2</sub> is the most extensively used photocatalyst. It has been regarded as an efficient photocatalyst for

degradation of organic pollutants from water due to its high stability, low cost and environmental friendliness [5,6]. However, UV-light is necessary to create the hole-electron pairs needed for the photocatalytic reaction which limits their use in environmental applications. Only 3–5% of UV in solar spectrum can be absorbed by pure TiO<sub>2</sub> due to its wide band gap (3.2 eV of anatase and 3.0 eV of rutile), which greatly restricts its photocatalytic applications in the visible-light range [7,8].

Therefore, to improve the efficiency of TiO<sub>2</sub> under solar (or visible) light is necessary to modify the material in order to facilitate the visible light absorption. Several approaches are made with this aim such as the introduction of doping agents or sensitizers to decrease the material band gap [9,10]. The introduction of metal doping agents into TiO<sub>2</sub> narrows the band gap by producing new hybrid states which confer significant visible light absorbance to TiO<sub>2</sub>. On the other hand, the improvement obtained using sensitizers is due to the direct absorption of visible light by the sensitizer and the release of electrons to TiO<sub>2</sub> in a redox process.

However, different problems were also detected. Metal doping shows thermal instability of doped TiO<sub>2</sub>, electron trapping by the metal centres decreasing the photocatalytic activity and high processing costs [11,12]. Alternatively, doping with non-metals such as N and S are used [13,14] being now the main drawbacks (i) the

\* Corresponding author.

E-mail address: [fjmaldon@ugr.es](mailto:fjmaldon@ugr.es) (F.J. Maldonado-Hódar).

difficulty to obtain N-doped  $\text{TiO}_2$  with high nitrogen concentration; (ii) the formation of defects which can act as recombination centres for carriers [15]; and (iii) the decrease of N concentration at the surface layer after irradiation [16].

The synergistic effect of the addition of carbon materials to  $\text{TiO}_2$  photocatalysts was initially presented using directly simple mixtures of both solids [17,18]. Although activated carbons were initially used to enhance the  $\text{TiO}_2$  photocatalytic performance [19], nanocarbons including carbon nanotubes (CNT) [18], nanohorns, fullerenes and graphene [20,21] have been combined with  $\text{TiO}_2$  by different approach for such objective. Carbon gels are a new type of nanocarbons [22] with high potential applications in catalysis due to their unique properties [23]. In spite that some carbon gels – $\text{TiO}_2$  composites were previously described [24], until our knowledge they have not been used today as photocatalysts.

The incorporation of carbon materials to the photocatalyst improve the  $\text{TiO}_2$  photoactivity by different mechanism [25]: (i) carbon absorbs over a wide range of visible light producing band-gap tuning/photosensitization, (ii) minimisation of electron/hole recombination and (iii) promotion of the reactants adsorption. The higher porosity of carbon facilitates the titania dispersion and the adsorption of reactants, enhancing the active site number and the contact between reactants and catalysts [25]. Additionally, carbon is a good electron acceptor. Electron transfers to the carbon phase minimize the electron/hole recombination on the  $\text{TiO}_2$ . Also the better dispersion of the semiconductor nanoparticles on the carbon phase reduce that recombination because mainly occurs at boundaries and defects [26]. Thus, if the particle size is reduced, the distance that the photogenerated electrons and holes need to travel through the surface reaction sites is reduced, thereby decreasing the recombination probability [27].

In this paper, new  $\text{TiO}_2$ -carbon composites were prepared by a sol-gel process and the xerogels obtained were deeply characterized and tested in the degradation of organic pollutants under visible light. The photocatalytic activity of the composites was evaluated using Orange G (OG) as a target molecule, and the relationship of the photocatalytic activity with the physicochemical characteristics of composites was studied. The prepared new materials present a high performance for the complete mineralization of pollutants (OG) under visible light.

## 2. Experimental

### 2.1. Synthesis of $\text{TiO}_2$ -carbon xerogel composites

$\text{TiO}_2$ -carbon xerogel composites were prepared by sol-gel synthesis using resorcinol-formaldehyde and titanium isopropoxide (IV) as carbon and titanium oxide precursor, respectively, in the presence of a non-ionic surfactant (Span 80). In a typical synthesis procedure, Span 80 (S) was dissolved in 900 mL of *n*-heptane and heated at 70 °C under reflux and stirring (450 rpm). Then a mixture containing resorcinol (R), formaldehyde (F) and water (W) was added dropwise into the above solution. Immediately after this addition, the proper amount of titanium isopropoxide was added drop by drop to the mixture. The molar ratio of the mixture was R/F = 1/2, R/W = 1/14 and R/S = 4.5.

The formed gel was aged at 70 °C for 24 h under stirring, and after that the suspension was filtered and the obtained solid, which displays an intense orange color, was placed in acetone (5 days, changing acetone twice daily) to exchange water within the pores by acetone. This procedure reduces the collapse of porosity during the subsequent drying process [28]. Then, the gel was filtered again and dried by microwave heating under argon atmosphere in periods of 1 min at 300 W until constant weight using a Saivod MS-287W microwave oven, according to previous results [28]. Pyrolysis

of organic xerogel-titanium oxide composites to obtain the corresponding carbon xerogel-titanium oxide composites was carried out at 900 °C in a tubular furnace using a  $\text{N}_2$  flow of 300 cm<sup>3</sup>/min, and a heating rate of 1 °C/min, in order to allow a soft removing of pyrolysis gases, and soaking time of 2 h at this temperature.

In this way, four  $\text{TiO}_2$ -carbon xerogel composites were prepared with different amount of titanium oxide (tentatively 10, 20, 30, and 40 wt% in the carbonized materials) by fitting the alkoxide ratio (assuming a weight loss during carbonization of 50%).  $\text{TiO}_2$ -carbon xerogel composites were refereed as CTiX (X corresponding to the theoretical percentage of titanium oxide present in the carbonized composite, e.g. CTi40 should contain 40% wt. of  $\text{TiO}_2$ ).

In order to make a comparison, carbon spheres covered by  $\text{TiO}_2$  were also synthesized. For that, the synthesis method was modified: the mixture of R, F and W was previously pre-gelled at 60 °C during the half of the time (2 h) needed to achieve the gel point. Then this pre-gelled mixture was added dropwise to a *n*-heptane solution containing Span 80 and maintained 1 h at 70 °C under reflux and stirring. This procedure permits the formation of organic xerogels structured in spheres which were finally coated with  $\text{TiO}_2$  by adding dropwise to the reactor the proper amount of titanium isopropoxide to obtain a  $\text{TiO}_2$  loading of 30 wt%. After dry and carbonization, following the procedure previously described, this sample was refereed as CTi30s2h.

A pure carbon xerogel (C100) prepared following the same sol-gel method used for CTi30s2h synthesis (but without Ti-alkoxide), P25 (from Degusa) and  $\text{TiO}_2$  anatase (From Sigma-Aldrich) were used as reference materials.

### 2.2. Characterization

Textural characterization was carried out by  $\text{N}_2$  and  $\text{CO}_2$  adsorption at –196 °C and 0 °C, respectively, using a Quantachrome Autosorb-1 equipment. The BET and Dubinin–Radushkevich equations were applied to determine the apparent surface area ( $S_{\text{BET}}$ ) and the micropore volume ( $W_0$ ), the mean micropore width ( $L_0$ ) and the microporous surface ( $S_{\text{mic}}$ ), respectively. Furthermore, the DFT method was used to calculate the mesopore volume of the samples ( $V_{\text{mes}}$ ). Pore size distributions were also obtained by applying the DFT method [29–32]. The total pore volume was considered as the volume of  $\text{N}_2$  adsorbed at  $P/P_0 = 0.95$  [33]. The morphology of supports was studied by scanning electron microscopy (SEM) using a LEO (Carl Zeiss) GEMINI-1530 microscope.

The titanium oxide phase was determined by powder X-ray diffraction (XRD) pattern using a Bruker D8 Advance X-ray diffractometer with  $\text{Cu K}\alpha$  radiation at a wavelength ( $\lambda$ ) of 1.541 Å. The  $2\theta$  angles were scanned from 20 to 70°. The average crystallite sizes ( $D$ ) were estimated by the Debye–Scherer equation,  $D = 0.95\lambda/\beta \cos \theta$ , where  $\theta$  is the diffraction angle and  $\beta$  is the full width at half-maximum (fwhm). The fwhm was determined with an extrapolated baseline between the beginning (low-angle side) and the end (high-angle side) of a diffraction peak with the highest intensity.

Optical absorption spectra of samples were obtained on a double-beam UV-vis spectrophotometer (CARY 5E from VARIAN) equipped with a Praying Mantis diffuse reflectance accessory (DRS). The reflectance spectra were analyzed according to the Kubelka–Munk (KM) method in order to calculate the band gap ( $E_g$ ) of samples. The graphic representations  $(F(R) \cdot h\nu)^n$  versus  $E = h\nu$  were used to calculate  $E_g$ ; where  $F(R)$  is a function of the reflectance;  $F(R) = (1-R)^2/2R$ ,  $R$  is the absolute reflectance of the sample layer and  $h\nu$  is the photon energy (eV), assuming also a value of  $n = 1/2$  for an indirect allowed transition and  $n = 2$  for a direct allowed transition. The  $E_g$  value was obtained by extrapolating the slope to  $a = 0$  according to the procedure used by López et al. [34].

Additional details of the theoretical approach and calculations were recently published [35].

### 2.3. Dye adsorption isotherms and kinetics

The orange G adsorption kinetics on photocatalysts were studied by recording the concentration decay curves in order to calculate the time required to reach the adsorption equilibrium at saturation. These experiments were carried out by placing 0.25 g of each sample in contact with 250 mL of Orange G solution (25 ppm) in a flask, this dispersion was maintained under shaking in a thermostatic bath at 298 K and aliquots were removed from the reactor at different times and filtered to determine their orange G concentration. The concentration of Orange G was measured by UV-vis spectrophotometry at 487 nm (5625 Unicam Ltd., Cambridge, UK) in the range indicating a linear relationship between absorbance and concentration. Adsorption kinetics shown the required time to reach the saturation equilibrium of maximum 3 h depending on sample used.

The Orange G adsorption isotherm on CTiX was carried out also in the same thermostatic bath at 298 K. For this, a volume of 25 mL with different initial concentrations (5–50 mg/L<sup>-1</sup>) of dye was placed in a flask and 0.025 g of sample was added. The flask was placed inside the thermostatic bath under shaking for 4 h to ensure the equilibrium are reached.

After reaching equilibrium, the adsorbed amount (q) from experimental data was calculated by the following equation:

$$q = \frac{V}{m}(C_0 - C_e)$$

where q is the adsorbed amount (mg/g), V the volume of solution (L), C<sub>0</sub> the initial Orange G concentration (mg/L), C<sub>e</sub> the equilibrium Orange G concentration (mg/L) and m is the amount of adsorbent (g).

Experimental data on the adsorption equilibrium of Orange G were interpreted using the adsorption isotherm models of Langmuir and Freundlich [36,37]. The Langmuir isotherm [36] is valid for monolayer adsorption onto a surface with a finite number of identical sites. It is given as the following equation:

$$q = \frac{q_m \cdot K_L \cdot C_e}{1 + K_L \cdot C_e}$$

where q is the amount of adsorbate adsorbed per specific amount of adsorbent (mg/g) and C<sub>e</sub> is equilibrium concentration (mg/L); q<sub>m</sub> relates to the maximum adsorption capacity (mg/g); K<sub>L</sub> is Langmuir equilibrium constant (L/mg). The linearized form of the Langmuir equation is

$$\frac{C_e}{q} = \frac{1}{q_m K_L} + \frac{C_e}{q_m}$$

q<sub>m</sub> and K<sub>L</sub> are determined from the linear plot of C<sub>e</sub>/q versus C<sub>e</sub>.

On the other hand, the Freundlich isotherm equation [37] is given as below:

$$q = K_F \cdot C_e^{1/n}$$

where K<sub>F</sub> is the relative adsorption capacity, n is relative with adsorption intensity so, (1/n) is an indicator of sorption intensity. If n lies between one and ten, this indicates a favorable sorption process [38]. The linearized form of the Freundlich equation is

$$\ln q = \ln K_F + \frac{1}{n} \ln C_e$$

The value of K<sub>F</sub> and n can be estimated from the intercept and slope of the linear plot of experimental data of ln q versus ln C<sub>e</sub>. The Freundlich isotherm provides no information on the monolayer adsorption density in comparison with the Langmuir model.

### 2.4. Photocatalytic reactor set-up and degradation procedure in presence of saturated photocatalysts

The photocatalytic activity of CTiX composites was compared in the OG degradation using a glass photoreactor (inner diameter of 8.5 cm x height of 20 cm) equipped with an inner tube of 2.5 cm of diameter placed in the reactor centre, allowing to fit a visible lamp of 14 W (ReptoLux 2.0) inside to ensure an uniform irradiation of all solution volume (Fig. 1). The degradation kinetic was follow by UV-spectrometry using a UV-vis spectrophotometer (5625 Unicam Ltd., Cambridge, UK), previously calibrated.

Before catalytic experiments, all the photocatalysts (800 mg) were saturated with the dye solution (800 mL) in dark to avoid the influence of the different adsorptive performance of each sample on the evolution of the dye concentration. This was carried out taking into account the previously results obtained (adsorption capacity and equilibrium time) from the kinetics and isotherms adsorption experiments. After saturation, the initial dye concentration (C<sub>0</sub>) was fitted in all cases to 10 mg/L, and then, visible light was turned on and this time was considered as the start degradation time. At a regular interval of 10 min, equal aliquot was removed from the reactor, filtered and the OG concentration measured by UV-spectrometry. The OG mineralization degree was followed by the evolution of total organic carbon (TOC) present in the solution during the photo-degradation experience using an analyzer Shimadzu V-CSH analyser with ASI-V autosampler and subtracting the inorganic carbon value in each sample from the total carbon value.

Finally, toxicity tests of solutions before and after catalytic degradation were performed using the normalized biotest (UNE/EN/ISO 11345-2) of luminescent inhibition of *Vibrio Fischeri* bacteria using the LUMIStox 300 system (Dr. LangeGmbH) with a LUMIStherm incubator. Toxicity was expressed as inhibition percentages at 15 min of exposure (I<sub>15</sub>) with reference to a stock saline solution used as control.

## 3. Results and discussion

The fraction of TiO<sub>2</sub> present in the CTiX carbon composites was determined by TGA, after burning the carbon phase in air flow. The TiO<sub>2</sub> percentages are slightly higher than the theoretical ones due to the fact that the weight lost during the carbonization is not exactly 50%, however the experimental data are much closed to the expected ones (Table 1). Morphology of sample was studied by scanning electron microscopy (Fig. 2). CTiX samples (Fig. 2a) show a typical structure of carbon xerogels [39] which consists in primary nanospheres connected between them to build a three-dimensional and porous structure. A homogeneous structure is obtained, without differentiation between the organic-inorganic phases. The EDX analysis of these samples showed an homogeneous Ti-distribution along all the sample independently of the TiO<sub>2</sub>-loading present in each composite (Fig. 2b and c)

However, after pregelification of the organic RF solution, isolated carbon microspheres were obtained (Fig. 2d). Evidently, pregelification provokes that the primary particle sizes obtained were larger. Microspheres of around 100 μm are obtained in this case, while the particle size of primary particles in CTiX samples are at the nanometer scale. TiO<sub>2</sub>-coated carbon microspheres are shown in Fig. 2e, and f, showing a more heterogeneous material; TiO<sub>2</sub>-coating shows different thicknesses. EDX spectra of a covered microsphere are also depicted in Fig. 2g, which clearly matches the recorded spectra.

These differences in the homogeneity of the samples were also pointed out when analyzing the thermal stability of composites in air flow. The TGA and DTG profiles of samples with similar TiO<sub>2</sub>-content (30%), composite CTi30 and coated CTi30s2h are compared

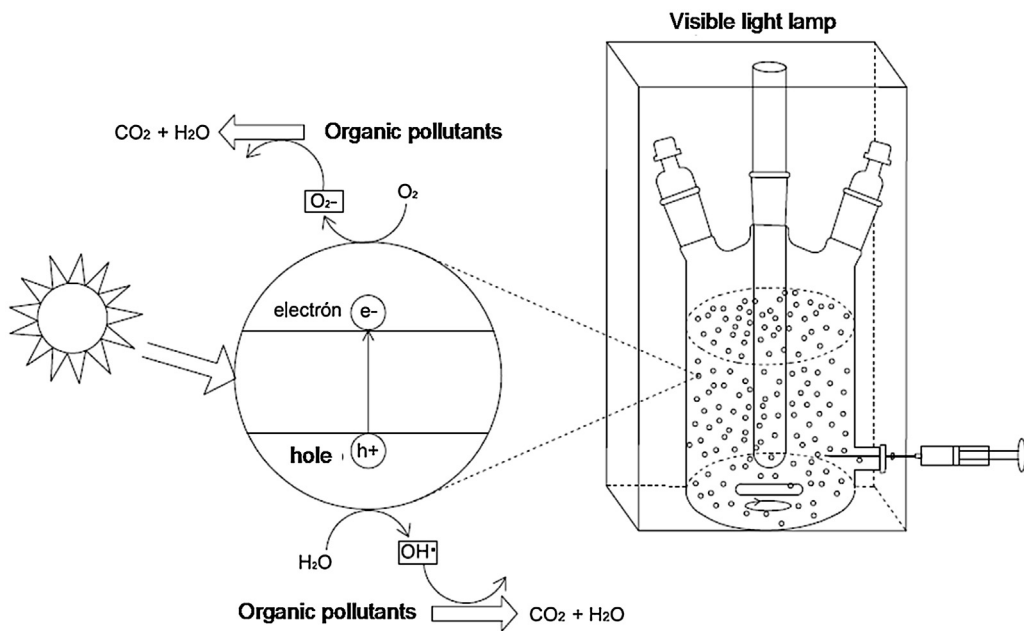


**Fig. 1.** Visible-light-assisted glass photoreactor used in the photodegradation reactions.

**Table 1**

Textural characteristics of the CTiX composites and reference materials.

Carbon	$S_{\text{BET}}$ $\text{m}^2 \text{g}^{-1}$	$W_0 (\text{N}_2) \text{ cm}^3 \text{g}^{-1}$	$W_0 (\text{CO}_2) \text{ cm}^3 \text{g}^{-1}$	$L_0 (\text{N}_2) \text{ nm}$	$L_0 (\text{CO}_2) \text{ nm}$	$V_{\text{mes}} \text{ cm}^3 \text{g}^{-1}$	$S_{\text{mic}} (\text{CO}_2) \text{ m}^2 \text{g}^{-1}$	$V_{0.95} \text{ cm}^3 \text{g}^{-1}$	$\text{TiO}_2 \%$
C100	571	0.226	0.275	0.76	0.56	0.100	856	0.330	0
CTi10	523	0.206	0.223	0.87	0.58	0.116	768	0.322	17
CTi20	480	0.190	0.205	0.76	0.56	0.203	737	0.393	22
CTi30	481	0.192	0.176	0.97	0.58	0.242	608	0.434	34
CTi30s2h	401	0.154	0.164	0.91	0.59	0.100	559	0.254	33
CTi40	586	0.227	0.174	1.21	0.62	0.438	562	0.665	45
P25	57	0.038	–	–	–	0.080	–	0.118	100

in Fig. 3. The carbon combustion starts at around 380 °C and is complete at around 650 °C in both cases. The TG-profiles are quite similar below 500 °C, but from this temperature, a delay is observed in the case of CTi30s2h. The minimum for CTi30 sample in the DTG profile at 500 °C corresponds to the maximum combustion rate, and this unique peak demonstrates the homogeneity and homogeneous distribution of the organic phase in the composite. The delay pointed out in the TG profile, and the appearance of a second peak in the DTG profile of CTi30s2h indicates the greater heterogeneity of the sample. Because the first minimum in the DTG profile is nearly coincident with the previously described for CTi30, the nature of the burned at this temperature organic phase should be also similar, in agreement with the similar recipe used. Thus, this first peak is associated to the uncoated or only partially coated carbon phase, while the second peak is associated to the burning of TiO<sub>2</sub>-coated carbon spheres, where the higher combustion temperature needed is induced by the slower diffusion of oxygen and the combustion gases to/from the interior of the coated spheres. In this sense, by integration of both peaks, 72.5% of spheres are covered by TiO<sub>2</sub>.

Due to the different morphology previously denoted by SEM, samples present porosity at different pore range. The pore structure of all photocatalysts was studied by nitrogen and carbon dioxide adsorption measurements, and results are also collected in Table 1. The results obtained from CO<sub>2</sub> and N<sub>2</sub> adsorption show a great variation of the textural properties between the composites. Increasing the % TiO<sub>2</sub>, the total porosity ( $V_{0.95}$ ) increases and is favored by a development of the volume of mesopores ( $V_{\text{mes}}$ ); a lineal relationship between both parameters is observed.

The micropore distribution can be analyzed by comparing the results from CO<sub>2</sub> and N<sub>2</sub>-adsorption experiments. It is well known that the CO<sub>2</sub> adsorption provides information about the narrow microporosity, corresponding to micropores with diameter lower than 0.7 nm, while the total microporosity is obtained from N<sub>2</sub> isotherm only in absence of diffusion restrictions. The microporosity determined by N<sub>2</sub> adsorption becomes wider ( $L_0 (\text{N}_2)$  increases) increasing the titanium oxide content while the ultramicroporosity ( $W_0 (\text{CO}_2)$ ) progressively decrease. In this sense, the  $S_{\text{BET}}$  of composites also decreased, because microporosity is mainly associated to the carbon phase, thus, this parameter is about ten times smaller for pure TiO<sub>2</sub> than for pure carbon xerogel. A linear decrease of  $W_0 (\text{N}_2)$ ,  $W_0 (\text{CO}_2)$  and  $S_{\text{mic}}$  is observed with increasing TiO<sub>2</sub> content. In this manner, at 20% of titanium oxide,  $W_0 (\text{N}_2) < W_0 (\text{CO}_2)$  denoting certain diffusion restrictions of N<sub>2</sub> into the microporosity, induced by the narrow microporosity of the predominant carbon phase, but increasing the TiO<sub>2</sub> content,  $W_0 (\text{N}_2) > W_0 (\text{CO}_2)$  as the consequence of the commented pore widening.

A high decrease of microporosity was obtained when carbon microspheres (C100) were covered by TiO<sub>2</sub> (CTi30s2h) due to the microporosity blockage by TiO<sub>2</sub>. Also, it is well-known that microporosity of carbon xerogels come from the intra-particle structure while meso and macroporosity are due to the voids inter-particles. Thus, no mesoporosity is obtained in CTi30s2h sample, which is formed by isolated carbon microspheres. On the contrary, mesoporosity is developed in CTi30 sample due to the smaller primary particle size and interconnected three-dimensional structure previously analyzed by SEM.

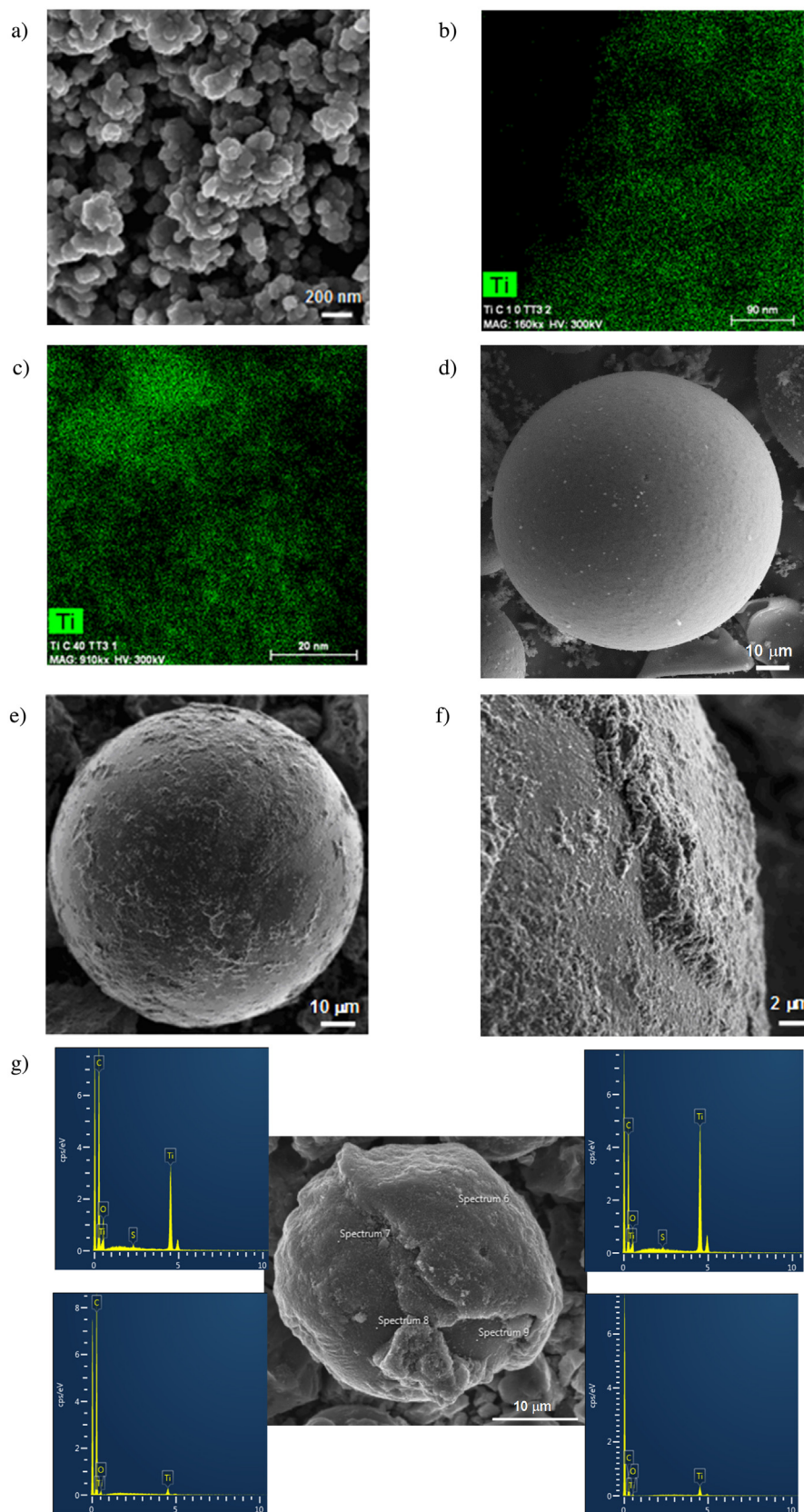


**Fig. 2.** Morphology of CTiX samples a) SEM images of CTi30, b) Ti-distribution determined by EDX on samples CTi10 and c) CTi40; d) SEM image of Ti30s2h, and e) surface detail of CTi30s2h and f) EDX analysis on selected points of a heterogeneously coated microsphere of CTi30s2h sample.

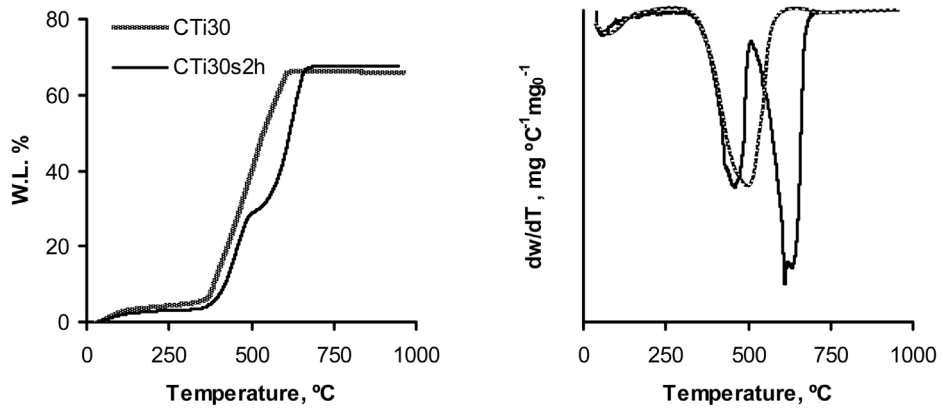


Fig. 3. TGA and DTG profiles of TiC30 and TiC30s2h.

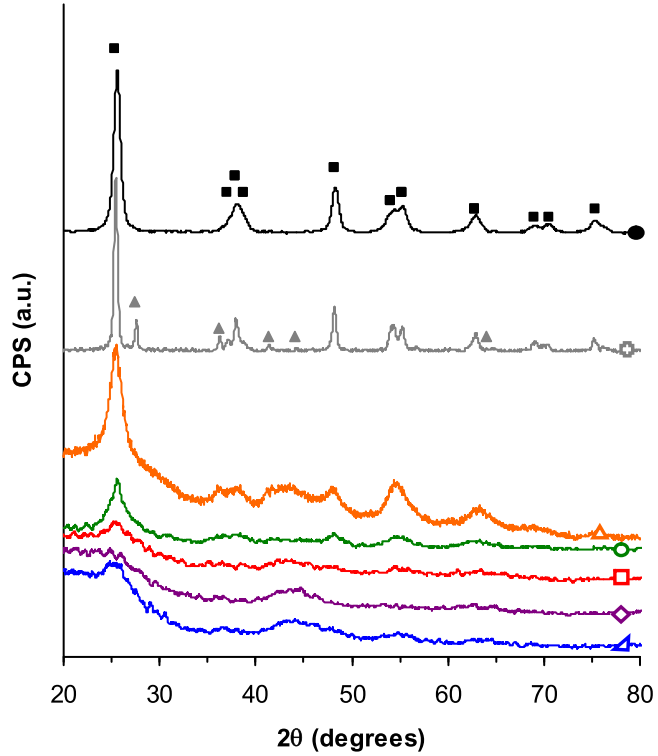


Fig. 4. Powder XRD patterns of samples: CTi10 ( $\blacktriangle$ ), CTi20 ( $\lozenge$ ), CTi30 ( $\square$ ), CTi40 ( $\circ$ ), CTi30s2h ( $\triangle$ ), P25 ( $\blacksquare$ ) and  $\text{TiO}_2$  anatase from alfa aesar ( $\bullet$ ). Anatase ( $\blacksquare$ ), Rutile ( $\blacktriangle$ ) crystalline structures.

Powder XRD measurements were performed in order to study the  $\text{TiO}_2$  crystallinity. As it is known,  $\text{TiO}_2$  can be present in two crystalline structures, anatase and rutile. Anatase is a metastable polymorphic form which transforms to rutile upon heating. For pure oxides, this transformation is fast at temperatures above 730 °C but has been shown to depend on impurity content, particle size, and surface area [40]. In previous manuscript, we demonstrated that the carbon phase difficult the crystal growth of the inorganic phase ( $\text{SiO}_2$ ,  $\text{Al}_2\text{O}_3$  or  $\text{TiO}_2$ ) in the corresponding C/oxide composite [24,41]. Fig. 4 shows XRD patterns obtained for the CTiX composites series. Below a  $\text{TiO}_2$  content of 30%, XRD patterns do not show any defined diffraction peak corresponding to the inorganic phase. For a  $\text{TiO}_2$  content of 40%, width and low intense diffraction peaks, corresponding to the anatase polymorphic form are observed. Due to the samples were carbonized at 900 °C, only rutile phase was to be expected in the final carbon-titanium oxide

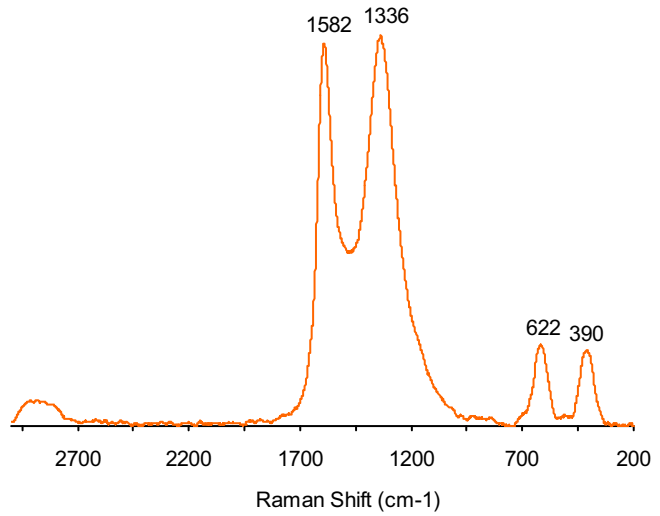


Fig. 5. Raman spectrum of composite CTi40.

composites. Nevertheless, only anatase phase was observed, and only at significantly high  $\text{TiO}_2$  content. These results point out that the  $\text{TiO}_2$  phase is well dispersed on the carbon matrix (as is also observed by SEM/EDX mapping), and that the interaction between both phases prevents the sintering of  $\text{TiO}_2$  nanoparticles and stabilizes the anatase polymorph in the carbon/ $\text{TiO}_2$  range studied, even at high carbonization temperature. However, when  $\text{TiO}_2$  is deposited on the organic xerogel microspheres the contact, and consequently the interactions between both phases are smaller. Thus, the influence of the carbon phase on the  $\text{TiO}_2$  properties is also smaller; larger anatase crystals, and even an incipient rutile formation, can be described from the CTi30s2h pattern, in comparison with the similar CTi30 composite.

The Raman spectroscopy was used to complement the crystallographic characterization of  $\text{TiO}_2$  in the composites. The Raman spectrum of sample CTi40 is shown in Fig. 5. Four bands were observed. The more intense bands, located at 1582 and 1336  $\text{cm}^{-1}$  correspond to the characteristics G and D of carbon materials [42]. The similar intensity of these bands ( $I_D/I_G = 1.02$ ) denotes the poor ordering (graphitization) of the carbon component. Two additional small bands are observed at 622 and 390  $\text{cm}^{-1}$  associated in this case to the  $\text{TiO}_2$  component. According to factor group analysis, six Raman transitions ( $1\text{A}_{1g}$ ,  $2\text{B}_{1g}$  and  $3\text{E}_g$ ) are allowed for anatase phase with bands located at 144, 197, 399, 513 and 639  $\text{cm}^{-1}$ . In the case of rutile, five Raman active modes ( $\text{B}_{1g}$ , multi-proton process,  $\text{E}_g$ ,  $\text{A}_{1g}$ ,  $\text{B}_{2g}$ ) located at 144, 446, 612 and 827  $\text{cm}^{-1}$ , are

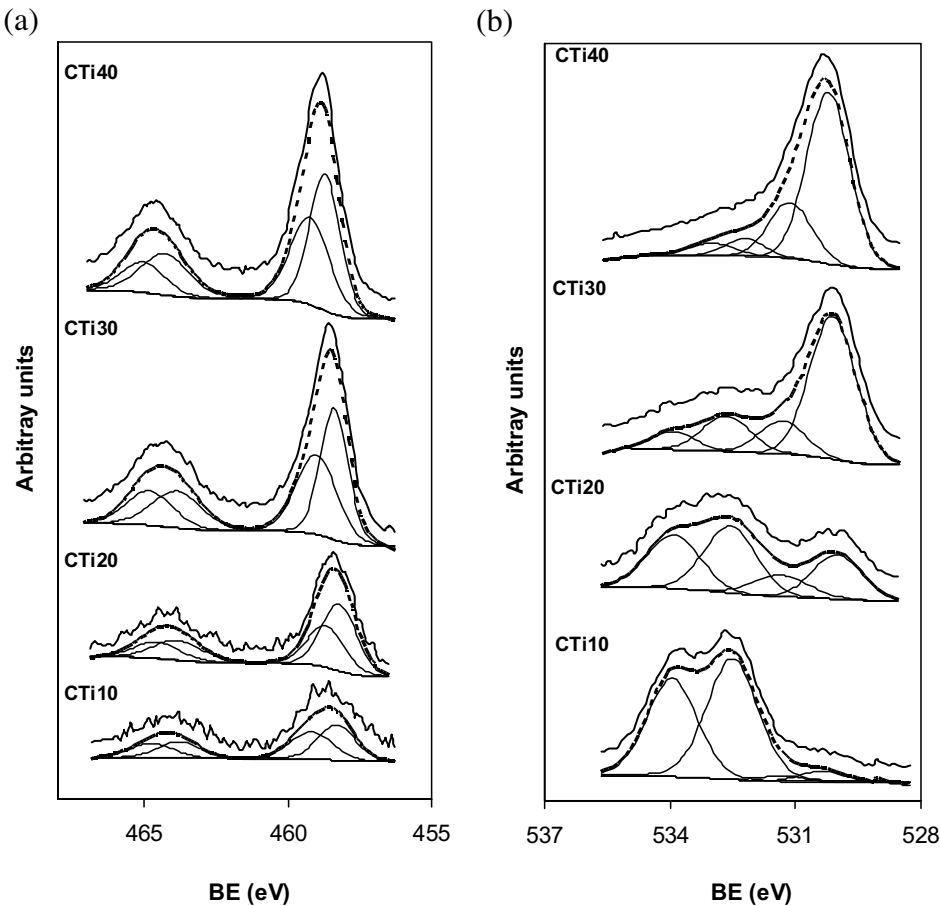


Fig. 6. XPS spectra of  $\text{TiO}_2$ -Carbon composites, a)  $\text{Ti}_{2p}$  and b)  $\text{O}_{1s}$  regions.

described [43,44]. Because bands in the CTi40 spectrum are shifted to lower frequencies regarding typical values (the carbon D-band appears at  $1350\text{ cm}^{-1}$ , and the anatase peaks  $E_g$  ( $635\text{ cm}^{-1}$ ) and  $B_{1g}$  ( $399\text{ cm}^{-1}$ )) we can conclude that the bands observed at  $622$  and  $390\text{ cm}^{-1}$  correspond to the anatase phase. The results of Raman spectroscopy and XRD do not provide evidences of rutile formation on CTi40. Taking into account that the carbon phase produces a delay in the anatase-rutile transformation, it is assumed a lower extent of this process in composites with smaller  $\text{TiO}_2$  contents.

The surface chemistry of samples was analysed by XPS. Results are collected in Table 2 and Fig. 6. The deconvolution of  $\text{Ti}_{2p}$  spectral region of  $\text{TiO}_2$  and P25 samples presents only one component at binding energy  $\text{BE} = 459.2\text{ eV}$ , corresponding to  $\text{Ti}^{4+}$ , in agreement to the BE values previously published [45]. However, in the case of composite samples two peaks were needed to fit this spectral region. The first one, at  $459.2\text{ eV}$ , corresponds to  $\text{Ti}^{4+}$  as is previously described and the peak at  $458.3\text{ eV}$  was assigned to  $\text{Ti}^{3+}$  [46]. This fact is due to the reducing character of the organic phase, but it is noteworthy that a similar  $\text{Ti}^{4+}$  reduction degree (at around 55%) is obtained for CTiX samples during carbonization independently of the  $\text{TiO}_2$  content. This result points out again the uniform distribution of  $\text{TiO}_2$  on the carbon phase when carbon/ $\text{TiO}_2$  composites are prepared. However, the reduction degree significantly decreases for sample CTi30s2h (until 41%), as consequence of the worse contact between both phases and the larger  $\text{TiO}_2$  crystal size of the coating, as previously discussed.

Two components, at  $530.8$  and  $532.2\text{ eV}$ , were used to fit the  $\text{O}_{1s}$  spectral region of  $\text{TiO}_2$  and P25 samples. The first one, and major component of  $\text{O}_{1s}$  spectral region, corresponds to the 'bulk' oxygen atom in the stoichiometric  $\text{TiO}_2$  form, while the high BE compo-

ment correspond to oxygen-containing surface functional groups, mainly hydroxyl ( $-\text{OH}$ ) groups were described [47,48]. However, four components were used to fit the  $\text{O}_{1s}$  spectral region of composites samples, due to the formation of different Ti-species and the oxygen linked to the carbon phase. Thus, as previously, the component at  $530.2\text{ eV}$  corresponds to oxygen bonded to  $\text{Ti}^{4+}$  while oxygen bonded to  $\text{Ti}^{3+}$  appears at  $531.3\text{ eV}$  [40]. On the other hand, the peaks at  $532.6$  and  $533.9\text{ eV}$  correspond to the oxygenated surface groups of the carbon phase, assigned respectively to  $\text{C}=\text{O}$  and  $\text{C}-\text{O}$  bonds. These two last peaks are predominant in the composites with low  $\text{TiO}_2$  content. In the case of composites with higher  $\text{TiO}_2$  content, the main components of the  $\text{O}_{1s}$  spectra are those corresponding to oxygen bonded to  $\text{Ti}^{4+}$  and  $\text{Ti}^{3+}$  species (see the deep change of their O profiles, Fig. 6). It is noteworthy that oxygenated surface groups of carbon materials can contribute to the dispersion and anchoring of  $\text{TiO}_2$  nanoparticles to the carbon surface, as have been recently pointed out [49]. Note also that Ti and O peaks appear in the composites at BE around  $0.7\text{ eV}$  higher than those detected for pure titania; this poorest electronic environment can be due to the ability of the carbon phase to accommodate electrons from the inorganic phase.

The electronic characteristics of samples were studied by diffuse reflectance analysis (Fig. 7) and band gap ( $E_g$ ) of samples were calculated using a modified Kubelka–Munk theory [34]. Theoretical and calculations details were recently published [35]. The calculated band gaps for pure P25,  $\text{TiO}_2$ , CTi30s2h and CTi30 samples were  $3.5\text{ eV}$ ,  $3.6\text{ eV}$ ,  $2.6$  and  $2.8\text{ eV}$ , respectively. P25 have a slightly lower band gap than  $\text{TiO}_2$  due to the presence of 25% of rutile phase which it is well known presents a lower band gap energy [50]. The small  $\text{TiO}_2$  particle size of TiC30 and the incipient rutile formation

**Table 2**

XPS results of composite samples: the surface titanium content, binding energy and percentage of the components used to fit the Ti<sub>2p</sub>, O<sub>1s</sub> and C<sub>1s</sub> spectral regions of CTiX composites.

Sample	BE (eV) C <sub>1s</sub>	Peak %	BE (eV) Ti <sub>2p</sub>	Peak %	BE (eV) O <sub>1s</sub>	Peak %	C <sub>XPS</sub> %Wt	O <sub>XPS</sub> %Wt	Ti <sub>XPS</sub> %Wt	O/Ti
TiO <sub>2</sub>	–	–	459.5	100	530.8 532.2	92 8	–	41.4	58.6	2.1
P25	–	–	459.5	100	530.7 532.2	92 8	–	45.4	54.6	2.5
CTi10	284.6 285.5 286.6 287.5 289.2 290.8	67 16 7 3 5 2	458.3 459.2	54 46	530.4 531.3 532.5 533.9	4 2 53 41	93.3	2.4	0.2	15.5
CTi20	284.6 285.6 286.6 287.5 289.2 290.6	73 14 5 2 3 2	458.2 459.0	59 41	530.0 531.3 532.6 533.9	23 12 36 29	94.6	4.0	1.4	8.5
CTi30	284.6 285.6 286.6 287.7 289.2 291.0	71 14 6 3 4 2	458.3 459.1	54 46	530.1 531.3 532.7 533.9	62 14 16 7	82.7	6.9	10.5	2.0
CTi30s2h	284.6 285.7 286.8 287.9 289.4 291.0	70 16 5 4 3 2	458.7 459.2	41 59	530.3 531.1 532.5 533.8	59 20 16 5	72.0	13.3	14.7	2.7
CTi40	284.6 285.5 287.0 288.6 289.9 291.1	70 14 7 4 3 2	458.3 459.2	55 45	530.2 531.1 532.2 533.0	67 22 6 5	73.3	11.8	15.0	2.4

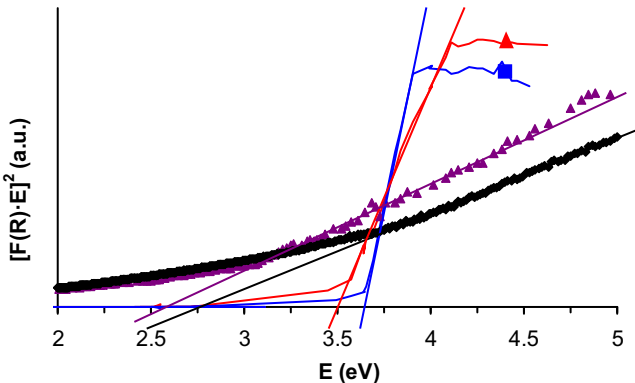


Fig. 7. Diffuse reflectance spectra of P25 (▲), TiO<sub>2</sub> (■), CTi30s2h (▲) and CTi30 (◆).

on TiC30s2h can contribute to the small differences observed. Also note that CTiX samples show smaller band gap as compared with both pure TiO<sub>2</sub>. These Eg values obtained from diffuse reflectance spectra results indicate that the performance of CTiX samples under visible radiation can be enhanced regarding pure TiO<sub>2</sub> phases. This redshift in CTiX samples band gap could be due to the quantum confinement experienced by the well dispersed TiO<sub>2</sub> on the carbon matrix [51]. Also, the presence of oxygen vacancies and/or partially reduced Ti sites detected by XPS act as new states localized in the band gap which could narrow the Eg and confer significant visible light absorbance to TiO<sub>2</sub>. These results are in agreement with those

recently published based on CNT-TiO<sub>2</sub> photocatalytic system used for water splitting [52].

### 3.1. Adsorption equilibrium studies

Orange G adsorption isotherms on CTiX composites are depicted in Fig. 8a. These isotherms were modeled using both Freundlich and Langmuir equations. The results obtained are given in Table 3. The maximum adsorption capacity ( $q_m$ ) of the composite increased in the order CTi10 < CTi20 < CTi30 < CTi40 (Table 3). These results point out an extended monolayer with increasing the titania content, which is related to the textural characteristics of the composites (Table 1). However, it is noteworthy that the adsorption capacity is not related with the micropore volume (in fact,  $q_m$  increases when  $W_0$  decreases), but with the mesopore one, denoting several diffusion restrictions of OG into the narrowest porosity. Fig. 8b shows the maximum adsorption capacity ( $q_m$ ) as a function of the adsorbents mesopore volume. A linear relationship is observed between both parameters, which denote a preferential adsorption of Orange G on the mesoporosity. Due to the kinetic size of Orange G ( $x = 5.44 \text{ \AA}$ ,  $Y = 10.14 \text{ \AA}$  and  $Z = 15.67 \text{ \AA}$ ) [53] and the micropore size on CTiX samples (maximum  $L_0 = 12.1 \text{ \AA}$  for CTi40), micropores do not play an important contribution in the Orange G adsorption. In fact, samples with similar  $V_{\text{meso}}$ , P25 and CTi30s2h, have similar Orange G adsorption capacity instead the higher micropores volume of the last one induced by the carbon phase.

Changing the composition of the composite not only the pore size distribution changes but also, the nature of the surface. The heterogeneity of the surface is tentatively discussed on the basis of

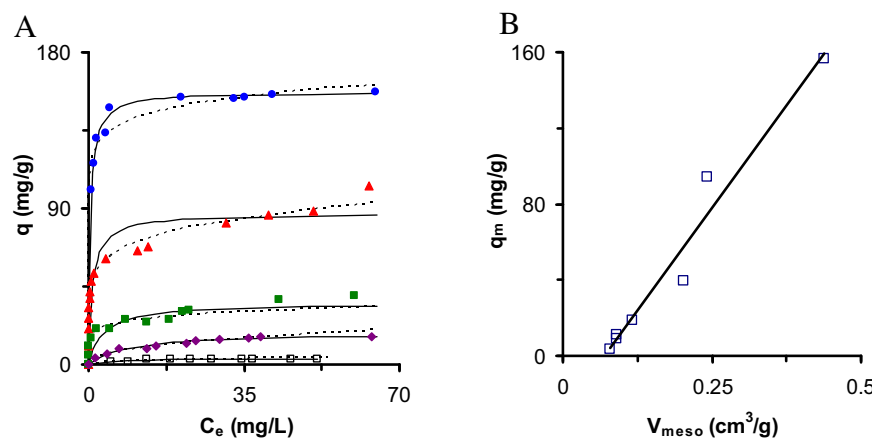


**Fig. 8.** a) Dashed line: Freundlich fitting and continuous line: Langmuir fittings. P25 (□), CTi10 (◆), CTi20 (■), CTi30 (▲) and CTi40 (●) b) Influence of the mesopore volume on the dye adsorption capacity of the samples.

**Table 3**

Results of application of the Langmuir equation to the adsorption isotherm of Orange G on pure oxides and CTiX composites at 298 K.

	P25	C100	CTi10	CTi20	CTi30	CTi30s2h	CTi40
<i>Langmuir isotherm</i>							
$q_m$ , (mg/g)	3.83	9.28	18.64	35.53	94.72	11.40	157.27
$K_L$ , (L/mg)	0.14	0.08	0.11	0.30	0.71	0.36	2.39
$R^2$	0.975	0.987	0.989	0.982	0.992	0.995	0.999
<i>Freundlich isotherm</i>							
$K_F$	0.75	1.25	3.46	17.92	48.94	3.61	115.10
$n$	2.39	2.01	2.39	6.70	6.48	2.93	9.98
$R^2$	0.871	0.989	0.988	0.977	0.990	0.907	0.962

the Freundlich results, because in this model many types of sites, with different affinity by the adsorbate (OG), are simultaneously working. This is related with the Freundlich exponent  $n$ , in such a manner that when  $n = 1$  the adsorption isotherm is lineal in the concentration range and the adsorption energy constant. The isotherm curvature is therefore consequence of the saturation of similar sites, and the Langmuir model can be then more appropriate. In fact, the linear regression coefficient values show that, in general, the Langmuir equation fitted much better the experimental data than Freundlich equation. In the case of the Langmuir model, the adsorption equilibrium constant  $K_L$  can be also related with the adsorption binding energy. Thus, after guaranteeing the accessibility of different molecules to the adsorption sites,  $K_L$  increases with the affinity for the adsorbate. It is noteworthy that the Freundlich exponent  $n$  also increases linearly with the  $TiO_2$  content ( $R^2 = 0.9$ ), indicating, as commented from the characterization results, a high homogeneity of the  $TiO_2$  nanoparticles distribution and nature. Also  $K_L$  increases in the same sense, but in this case a deep increase is observed in the case of CTi40, which can be related also with a more opened microporosity (Table 1).

### 3.1.1. Photocatalytic activity

The photocatalytic activity of CTiX composites was evaluated towards the degradation of the same industrial textile dye, namely Orange G (OG), under a low power (14 W) artificial visible light. Samples were previously saturated with OG, according the previous results, in order to avoid adsorption interferences. Both pure phases, P25 and C100 were also used as reference materials. Fig. 9a shows the removal of OG as a function of the irradiation time. As it can be seen, no degradation is obtained without using catalyst (photolysis) as well as using the carbon xerogel (C100). An increase in the OG degradation is observed increasing the amount of  $TiO_2$  in the composite, being the OG removed 37, 62, 79, 90% at 400 min of reaction for CTi10, CTi20, CTi30 and CTi40, respectively. Thus,

it was found that among the synthesized catalysts, CTi40 decolorized the dye to the largest extent. Only the composite with the smaller  $TiO_2$  content (CTi10) showed a worse performance than commercial P25, which only reach a 43% of removal after 400 min of reaction. Due to the samples were previously saturated in dark, this increased performance is not related with a higher adsorption capacity.

CTiX composites are more efficient than the pure  $TiO_2$  samples. These data show that there is a very high synergic effect between carbon xerogel and  $TiO_2$  improving the photoactivity of the pure samples and, what is more important, turning them into active catalysts under visible light even instead the low lamp power (14 W). These results can be related with the band gap of each sample. Considering the emission spectrum of the visible lamp used (Fig. 9b) it can be observed that around 2% of the emitted radiation has a higher energy than the P25 band gap, allowing some photocatalytic effect of this sample on the OG degradation. Due to the lowest band gap of CTiX materials, the higher photocatalytic activity of these materials on the visible range can be also related with its higher visible absorption capacity.

The band gap decrease in CTiX materials could be related with the presence of the oxygen vacancies shown by XPS. Oxygen vacancies have important impacts on the electronic properties of  $TiO_2$  leading to a shifting of the band gap to lower energy range. In this sense, Nakamura et al. [54] ascribed the appearance of the visible light activity in plasma-treated  $TiO_2$  photocatalyst to the newly formed oxygen vacancy state between the valence and the conduction bands in the  $TiO_2$  band structure. The oxygen vacancy states in anatase  $TiO_2$  were determined to be located 2.02–2.45 eV above the valence band. Similar results were observed by Yan et al. [55]. These authors describe the formation of vacancies in both anatase or rutile phases by annealing the samples at different temperatures and found a direct correlation between the photocatalytic activi-

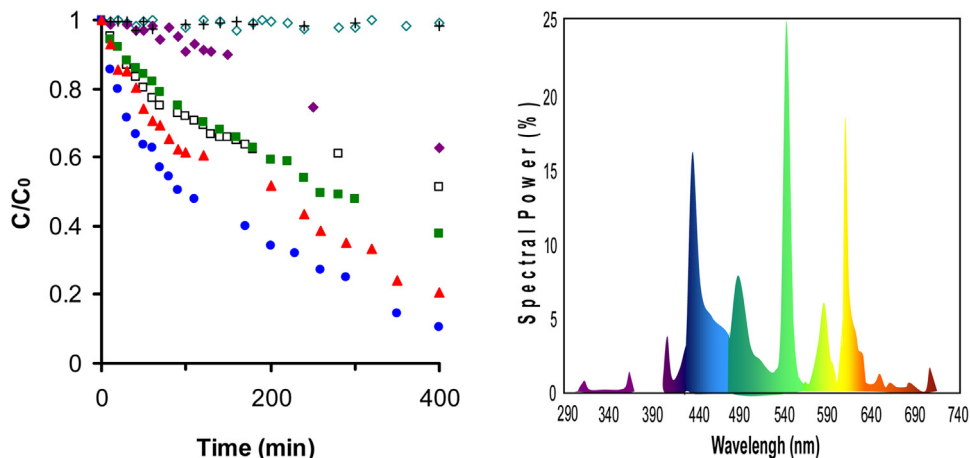


**Fig. 9.** Left: Kinetic of Orange G photocatalytic degradation and Right: lamp emission spectrum. C100 ( $\diamond$ ), CTi10 ( $\blacklozenge$ ), photolysis (+), P25 ( $\square$ ), CTi20 ( $\blacksquare$ ), CTi30 ( $\blacktriangle$ ) and CTi40 ( $\bullet$ ).

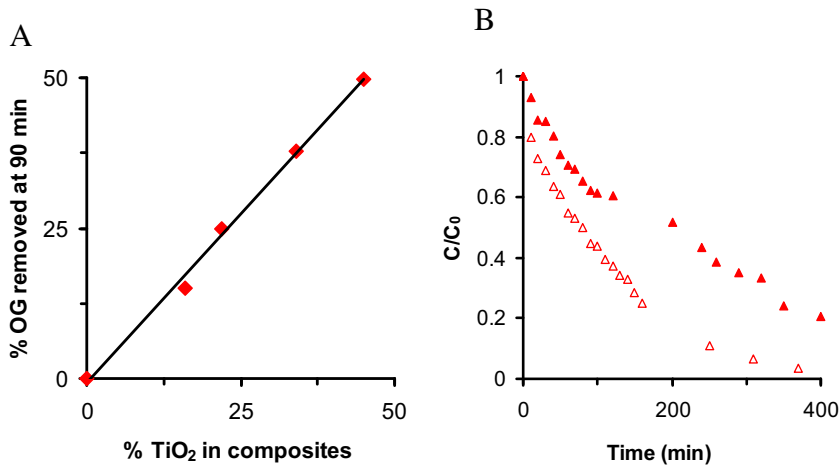


**Fig. 10.** a) % OG removed at 90 min as a function of%  $\text{TiO}_2$  in the composites and b) kinetic of OG photocatalytic degradation of CTi30 ( $\blacktriangle$ ) and CTi30s2h ( $\triangle$ ).

ity and the defect density. Oxygen vacancy clusters enhance the activity for the photooxidation of  $\alpha$ -phenethyl alcohol.

Nevertheless, additional factors could contribute to this enhanced behaviour. As showed by SEM or XRD,  $\text{TiO}_2$  is well dispersed onto carbon matrix. Due to this good dispersion and contact between the carbon matrix and  $\text{TiO}_2$  nanoparticles, the flow of electrons amidst the carbon matrix and conduction band of  $\text{TiO}_2$  is increased (as is detoned by BE values in XPS). This synergistic effect between these components effectively reduces the recombination of electron-holes leading to the increased charge carrier separation with a significant increase of the photoactivity.

When compare the performance of CTiX catalysts, a linear correlation between the  $\text{TiO}_2$  content and the reached OG degradation is obtained (Fig. 10a). This fact confirms again the homogeneous distribution of  $\text{TiO}_2$  nanoparticles along the carbon matrix in all the samples, and the homogenous surface chemistry of these nanoparticles. Nevertheless, when compare the performance of CTi30s2h and CTi30 samples (Fig. 10b), both with a similar  $\text{TiO}_2$  content, a best behaviour is observed for CTi30s2h in spite of the smaller  $\text{TiO}_2$  reduction degree (Table 2) and the larger crystal size in this case. However, the photocatalytic performance is favoured by the higher  $\text{TiO}_2$  content on surface (Table 2) also induced by the preparation method. In the case of CTi30 sample some  $\text{TiO}_2$  particles could be embedded on carbon matrix and not be accessible to OG degradation. Additionally, this sam-

ple presents an incipient rutile formation. As it is well known, anatase is more active than rutile instead its higher band gap (3.2 vs 3.0 eV for anatase and rutile, respectively). Preferential diffusion of excitons along certain crystallographic directions has been proposed to be important to explain surface orientation dependencies in their oxidation/reduction behaviour [56]. However, a mixture of anatase-rutile (as in the case of P25) makes better photocatalyst than pure anatase. Such a mixture of phases seem to effectively transfer photo-excited electrons from the conduction band of anatase to that of rutile, favouring electron-hole separation and enhancing the visible light photocatalytic activity [57]. Thus, the partial anatase – rutile transformation can also favour the photocatalytic activity of CTi30s2h sample.

Finally, we must consider not only the OG degradation obtaining a colourless solution, but also the total pollutant mineralization degree to  $\text{CO}_2$  avoiding the formation of intermediate oxidation compounds and the toxicity of this solution. The total organic carbon (TOC) concentration was measured and compared with the TOC calculated according the OG concentration determined by UV at each reaction time (Fig. 11). As observed, although decolourization is initially faster, after around 180 min of reaction both TOC and decolourization present similar values, indicating that Orange G is completely mineralized. Also, toxicity showed the same tendency. This fact indicates that photodegradation of Orange G is complete to  $\text{CO}_2$ , progressively reducing the toxicity of the treated

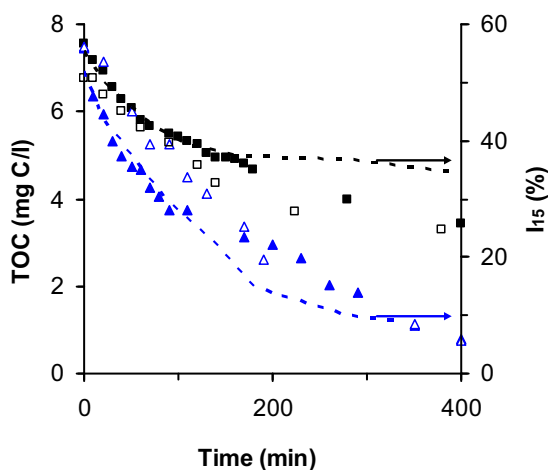


**Fig. 11.** Variation of the Total Organic Carbon concentration and toxicity of solution treated with ▲ CTi40, ■ P25. Close symbol (from UV data) open Symbol (TOC measurement); line: Toxicity tests ( $I_{15}$ ).

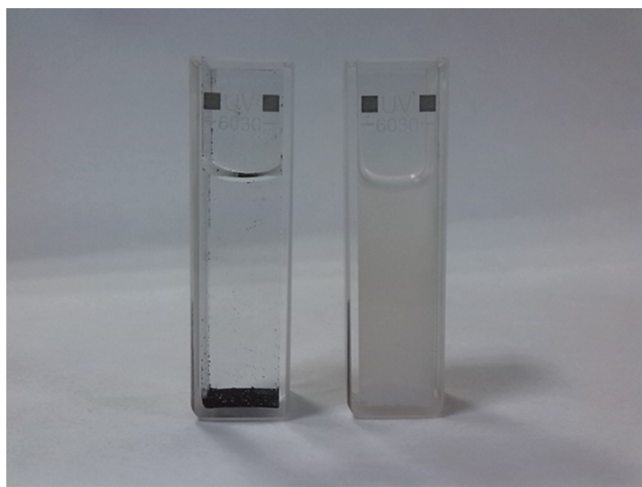


**Fig. 12.** Suspensions of the photo-catalysts after reaction. Left (CTi30s2h); right (P25).

water. Toxicity was determined according to the inhibition of *Vibrio Fischeri* bacteria degree, as described in the experimental section. After 400 min of reaction, the toxicity ( $I_{15}$ ) of the solution treated with CTi40 is close to zero, while is significantly high for the solution treated with P25. As consequence, it is important remark that CTiX composites are new advanced materials which not only permit the change of UV radiation by visible light during photo-catalytic reactions but, more importantly, are able to mineralize completely the dye avoiding the formation intermediate pollutant products, in such a manner that the toxicity of water is also removed.

In industrial applications, the separation and recovering of the catalyst after the water treatment must be also considered. The easy recuperation of the catalysts favours the catalyst reuse and reduces the separation costs. Thus, in some cases special properties like the magnetic behaviour is induced by doping with metal (Fe) to favour the separation process [58]. In this case, the composite easily precipitates by itself after turning off the stirring, making possible an easy separation from the media after reaction, while commercial P25 remain in suspension needing an additional centrifugation process (Fig. 12).

#### 4. Conclusions

Carbon xerogel-TiO<sub>2</sub> composites (CTiX) were successfully synthesized by sol-gel techniques. Composites present a homogeneous and three-dimensional mesoporous structure, where both phases are also homogeneously and intimately distributed. This procedure can be fitted to obtain TiO<sub>2</sub> coating the carbon phase structured microspheres, obtaining microporous materials. Due to the interactions between both phases all composites present a high dispersion of anatase TiO<sub>2</sub> nanoparticles on the carbon support in spite that samples are carbonized a 900 °C. These nanoparticles are partially reduced, with an oxygen surface distribution highly dependent on the TiO<sub>2</sub> content. However, the smaller contact between both phases in coated carbon particles favours the crystallinity of anatase and the incipient transformation to rutile. This interaction also provoke that the band gaps of the CTiX samples are lower than 2.8 eV, making then excellent photocatalysts under visible light. An industrial textile dye, Orange G, was selected as target molecule. The OG adsorption is controlled by the mesopore volume, and consequently favoured on CTiX regarding coated samples. CTiX also showed a high efficiency in the OG photodegradation under visible light due to the synergistic effect between organic and inorganic phases, being more effective than commercial samples of pure TiO<sub>2</sub>. This better behaviour could be related with different properties of the composites: i) the organic matrix favour the titania reduction during carbonization. Oxygen vacancies plays an important role on the catalytic performance, producing new hybrid states in the band gap, which narrows the band gap and confer significant visible light absorbance, ii) carbon phase favour the electron transfer from TiO<sub>2</sub> nanoparticles, reducing the charge carriers recombination, iii) carbon phase avoid the sintering of titania nanoparticles and the transformation to the less active rutile phase. In these small TiO<sub>2</sub> nanoparticles, the distance that the photogenerated electrons and holes need to travel to surface reaction sites is reduced, thereby reducing also the recombination probability. TiO<sub>2</sub>-coated photocatalyst present even an improved performance, favoured by the greater accessibility of pollutant to the TiO<sub>2</sub> active centers, and an additional synergistic effect between rutile-anatase phases.

#### Acknowledgements

EBG acknowledges for a pre-doctoral fellowship to the MCINN project CTM2010-18889. This research is supported by the FEDER and Spanish projects CTQ2013-44789-R (MINECO) and P12-RNM-2892 (Junta de Andalucía).

#### References

- [1] F. Rojas-Serrano, J.I. Pérez, M.Á. Gómez, Chem. Eng. Process. 105 (2016) 21–29.
- [2] B.M. Esteves, C.S.D. Rodrigues, R.A.R. Boaventura, F.J. Maldonado-Hódar, L.M. Madeira, J. Environ. Manag. 166 (2016) 193–203.
- [3] R.S. Ribeiro, A.M.T. Silva, J.L. Figueiredo, J.L. Faria, H.T. Gomes, Appl. Catal. B: Environ. 187 (2016) 428–460.
- [4] J. Guzmán, R. Mosteo, J. Sarasá, J.A. Alba, J.L. Ovelleiro, Sep. Purif. Technol. 164 (2016) 155–162.
- [5] H. Kazuhito, I. Hiroshi, F. Akira, Jpn. J. Appl. Phys. 44 (2005) 8269.
- [6] H. Kim, G.H. Moon, D. Monllor-Satoca, Y. Park, W. Choi, J. Phys. Chem. C 116 (2012) 1535–1543.
- [7] M. Pelaez, N.T. Nolan, S.C. Pillai, M.K. Seery, P. Falaras, A.G. Kontos, P.S.M. Dunlop, J.W.J. Hamilton, J.A. Byrne, K. O'Shea, M.H. Entezari, D.D. Dionysiou, Appl. Catal. B: Environ. 125 (2012) 331–349.
- [8] W. Ren, Z. Ai, F. Jia, L. Zhang, X. Fan, Z. Zou, Appl. Catal. B: Environ. 69 (2007) 138–144.
- [9] J. Zhang, Y. Wu, M. Xing, S.A.K. Leghari, S. Sajjad, Energy Environ. Sci. 3 (2010) 715–726.
- [10] S. Lee, Y. Lee, D.H. Kim, J.H. Moon, ACS Appl. Mater. Interfaces 5 (2013) 12526–12532.
- [11] Y. Wang, H. Cheng, Y. Hao, J. Ma, W. Li, S. Cai, Thin Solid Films 349 (1999) 120–125.
- [12] H. Yamashita, M. Honda, M. Harada, Y. Ichihashi, M. Anpo, T. Hirao, N. Itoh, N. Iwamoto, J. Phys. Chem. B 102 (1998) 10707–10711.

[13] Y. Izumi, T. Itoi, S. Peng, K. Oka, Y. Shibata, *J. Phys. Chem. C* 113 (2009) 6706–6718.

[14] C. Di Valentini, E. Finazzi, G. Pacchioni, A. Selloni, S. Livraghi, M.C. Paganini, E. Giannello, *Chem. Phys.* 339 (2007) 44–56.

[15] H. Irie, Y. Watanabe, K. Hashimoto, *J. Phys. Chem. B* 107 (2003) 5483–5486.

[16] M. Kitano, K. Funatsu, M. Matsuoka, M. Ueshima, M. Anpo, *J. Phys. Chem. B* 110 (2006) 25266–25272.

[17] J. Matos, J. Laine, J.M. Herrmann, *Appl. Catal. B: Environ.* 18 (1998) 281–291.

[18] W. Wang, P. Serp, P. Kalck, J.L. Faria, *Appl. Catal. B: Environ.* 56 (2005) 305–312.

[19] G. Li Puma, A. Bono, D. Krishnaiah, J.G. Collin, *J. Hazard Mater.* 157 (2008) 209–219.

[20] S. Morales-Torres, L.M. Pastrana-Martínez, J.L. Figueiredo, J.L. Faria, A.M.T. Silva, *Appl. Surf. Sci.* 275 (2013) 361–368.

[21] M.J. Sampaio, C.G. Silva, A.M.T. Silva, L.M. Pastrana-Martínez, C. Han, S. Morales-Torres, J.L. Figueiredo, D.D. Dionysiou, J.L. Faria, *Appl. Catal. B: Environ.* 170–171 (2015) 74–82.

[22] M. Inagaki, K. Kaneko, T. Nishizawa, *Carbon* 42 (2004) 1401–1417.

[23] F.J. Maldonado-Hódar, *Catal. Today* 218–219 (2013) 43–50.

[24] F.J. Maldonado-Hódar, C. Moreno-Castilla, J. Rivera-Utrilla, *Appl. Catal. A: Gen.* 203 (2000) 151–159.

[25] R. Leary, A. Westwood, *Carbon* 49 (2011) 741–772.

[26] W. Li, C. Ni, H. Lin, C.P. Huang, S.I. Shah, *J. Appl. Phys.* 96 (2004) 6663–6668.

[27] F. Cui, L. Xu, T. Cui, T. Yao, J. Yu, X. Zhang, K. Sun, *RSC Adv.* 4 (2014) 33408–33415.

[28] E. Gallegos-Suárez, A.F. Pérez-Cadenas, F.J. Maldonado-Hódar, F. Carrasco-Marín, *Chem. Eng. J.* 181–182 (2012) 851–855.

[29] S. Brunauer, P.H. Emmett, E. Teller, *J. Am. Chem. Soc.* 60 (1938) 309–319.

[30] M.M. Dubinin, *Carbon* 23 (1985) 373–380.

[31] M.M. Dubinin, *Russ. J. Phys. Chem.* 39 (1965) 1305–1317.

[32] F. Stoeckli, In: *Porosity in Carbons—Characterization and Applications*, Arnold, London, 1995.

[33] R. Ubago-Pérez, F. Carrasco-Marín, D. Fairén-Jiménez, C. Moreno-Castilla, *Microporous Mesoporous Mater.* 92 (2006) 64–70.

[34] R. López, R. Gómez, *J. Sol-Gel Sci. Technol.* 61 (2012) 1–7.

[35] F. Orellana-García, M.A. Álvarez, M.V. López-Ramón, J. Rivera-Utrilla, M. Sánchez-Polo, M.Á. Fontecha-Cámarra, *Appl. Catal. B: Environ.* 181 (2016) 94–102.

[36] I. Langmuir, *J. Am. Chem. Soc.* 40 (1918) 1361–1403.

[37] C.H. Yang, *J. Colloid Interface Sci.* 208 (1998) 379–387.

[38] A.O. Dada, A.P. Olalekan, A.M. Olatunyu, O. Dada, *IOSR J. Appl. Chem.* 3 (2012) 38–45.

[39] C. Moreno-Castilla, F.J. Maldonado-Hódar, *Carbon* 43 (2005) 455–465.

[40] D. Hanaor, C. Sorrell, *J. Mater. Sci.* 46 (2011) 855–874.

[41] C. Moreno-Castilla, F.J. Maldonado-Hódar, *Phys. Chem. Chem. Phys.* 2 (2000) 4818–4822.

[42] F.J. Maldonado-Hódar, C. Moreno-Castilla, J. Rivera-Utrilla, Y. Hanzawa, Y. Yamada, *Langmuir* 16 (2000) 4367–4373.

[43] J. Yan, G. Wu, N. Guan, L. Li, Z. Li, X. Cao, *Phys. Chem. Chem. Phys.* 15 (2013) 10978–10988.

[44] T. Potlog, M. Dobromir, D. Luca, P. Onufrijevs, A. Medvids, A. Shamardin, *Curr. Appl. Phys.* 16 (2016) 826–829.

[45] A.R. Gonzalez-Elipe, P. Malet, J.P. Espinós, A. Caballero, G. Munuera, *Stud. Surf. Sci. Catal.* 48 (1989) 427–436.

[46] A.R. González-Elipe, A. Fernández, J.P. Espinós, G. Munuera, *J. Catal.* 131 (1991) 51–59.

[47] M.E. Nagassa, A.E. Daw, W.G. Rowe, A. Carley, D.W. Thomas, R. Moseley, *Clin. Oral Implants Res.* 19 (2008) 1317–1326.

[48] A. Samokhvalov, E.C. Duin, S. Nair, B.J. Tatarchuk, *Surf. Interface Anal.* 42 (2010) 1476–1482.

[49] L.M. Pastrana-Martínez, S. Morales-Torres, V. Likodimos, P. Falaras, J.L. Figueiredo, J.L. Faria, A.M.T. Silva, *Appl. Catal. B: Environ.* 158–159 (2014) 329–340.

[50] T. Luttrell, S. Halpegamage, J. Tao, A. Kramer, E. Sutter, M. Batzill, *Sci. Rep.* (2014) 4043.

[51] S. Monticone, R. Tufeu, A.V. Kanaev, E. Scolan, C. Sanchez, *Appl. Surf. Sci.* 162–163 (2000) 565–570.

[52] A. Moya, A. Cherevan, S. Marchesan, P. Gebhardt, M. Prato, D. Eder, J.J. Vilatela, *Appl. Catal. B: Environ.* 179 (2015) 574–582.

[53] X. Zhao, X. Bu, T. Wu, S.T. Zheng, L. Wang, P. Feng, *Nat. Commun.* 4 (2013) 1–9.

[54] I. Nakamura, N. Negishi, S. Kutsuna, T. Ihara, S. Sugihara, K. Takeuchi, *J. Mol. Catal. A: Chem.* 161 (2000) 205–212.

[55] J. Yan, G. Wu, N. Guan, L. Li, Z. Li, X. Cao, *Phys. Chem. Chem. Phys.* 15 (2013) 10978–10988.

[56] T. Luttrell, S. Halpegamage, J. Tao, A. Kramer, E. Sutter, M. Batzill, *Sci. Rep.* 4 (2014) 4043–4051.

[57] V. Etacheri, M.K. Seery, S.J. Hinder, S.C. Pillai, *Chem. Mater.* 22 (2010) 3843–3853.

[58] S. Xu, W. Shangguan, J. Yuan, M. J. Shi Chen, *Appl. Catal. B: Environ.* 71 (2007) 177–184.